

# Gate-Tunable Transport in Quasi-One-Dimensional $\alpha$ -Bi<sub>4</sub>I<sub>4</sub> Field Effect Transistors

Yulu Liu, Ruoyu Chen, Zheneng Zhang, Marc Bockrath, Chun Ning Lau,\* Yan-Feng Zhou, Chiho Yoon, Sheng Li, Xiaoyuan Liu, Nikhil Dhale, Bing Lv,\* Fan Zhang,\* Kenji Watanabe, Takashi Taniguchi, Jianwei Huang, Ming Yi,\* Ji Seop Oh, and Robert J. Birgeneau\*



Cite This: *Nano Lett.* 2022, 22, 1151–1158



Read Online

ACCESS |

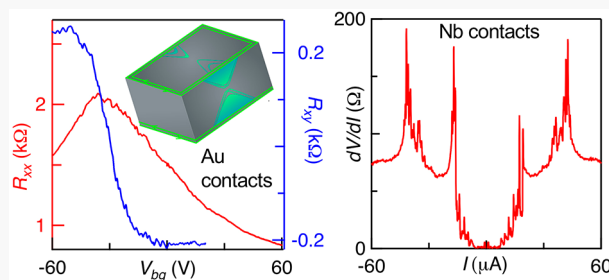
Metrics & More

Article Recommendations

Supporting Information

**ABSTRACT:** Bi<sub>4</sub>I<sub>4</sub> belongs to a novel family of quasi-one-dimensional (1D) topological insulators (TIs). While its  $\beta$  phase was demonstrated to be a prototypical weak TI, the  $\alpha$  phase, long thought to be a trivial insulator, was recently predicted to be a rare higher order TI. Here, we report the first gate tunable transport together with evidence for unconventional band topology in exfoliated  $\alpha$ -Bi<sub>4</sub>I<sub>4</sub> field effect transistors. We observe a Dirac-like longitudinal resistance peak and a sign change in the Hall resistance; their temperature dependences suggest competing transport mechanisms: a hole-doped insulating bulk and one or more gate-tunable ambipolar boundary channels. Our combined transport, photoemission, and theoretical results indicate that the gate-tunable channels likely arise from novel gapped side surface states, two-dimensional (2D) TI in the bottommost layer, and/or helical hinge states of the upper layers. Markedly, a gate-tunable supercurrent is observed in an  $\alpha$ -Bi<sub>4</sub>I<sub>4</sub> Josephson junction, underscoring the potential of these boundary channels to mediate topological superconductivity.

**KEYWORDS:** quasi-1D topological insulator, Bi<sub>4</sub>X<sub>4</sub>, Josephson transistor, topological superconductivity



Topological insulators (TIs) are insulating in the bulk yet conducting on the boundary, protected by symmetry and immune to disorder.<sup>1,2</sup> They enable near-perfect devices using imperfect interfaces for breakthrough technologies. Their discovery has led to an ongoing revolution, deepening our fundamental understanding in condensed matter and materials physics. Over the past decade, there has been rapidly growing interest in the search for TI materials.<sup>3–11</sup> Thus far, most of them are either three-dimensional (3D) strongly bonded bulk materials in the first generation, e.g., Bi<sub>1-x</sub>Sb<sub>x</sub> alloys with rather complicated surface states,<sup>12,13</sup> or quasi-two-dimensional (2D)-layered van der Waals materials in the second generation, e.g., the Bi<sub>2</sub>Se<sub>3</sub> family compounds with only one surface Dirac cone.<sup>14–16</sup> Recently, for the search of the rare weak TIs, first-principles calculations predicted a new generation of TI materials Bi<sub>4</sub>I<sub>4</sub> and Bi<sub>4</sub>Br<sub>4</sub> in a quasi-one-dimensional (1D) geometry, which uniquely harbor two natural cleavage surfaces and feature two Dirac cones at only one of the cleavage surfaces.<sup>3</sup> They promise several advantages, such as multiple cleavage planes, strain-induced phase transitions between weak TI, strong TI, and trivial insulator states, and hosting of prototypical higher order TIs with helical hinge modes.<sup>3–8</sup> As shown in Figure 1a, Bi<sub>4</sub>I<sub>4</sub> is composed of a periodic stack of atomic chains aligned in the *b* direction,<sup>17–19</sup> with very weak interlayer binding energies for the (100) and (001) planes.<sup>3,17</sup> In each unit cell, the two internal Bi atoms form zigzag chains,

while the two external Bi atoms are each bonded to four I atoms and one internal Bi atom. The crystals have two independent symmetries: spatial inversion and (010) mirror reflection.

Bi<sub>4</sub>I<sub>4</sub> has two structural phases,  $\alpha$  and  $\beta$ , which crystallize in the same space group *C2/m* yet mainly<sup>6</sup> differ in the way their (001) monolayers are stacked.<sup>17–19</sup> In Bi<sub>4</sub>I<sub>4</sub>, an important structural phase transition at  $\sim$ 300 K between the two phases has been observed.<sup>5,7,20</sup> More notably, the weakly coupled Bi<sub>4</sub>I<sub>4</sub> (001) monolayers are 2D TIs<sup>6</sup> (Figure 1d), although each monolayer may relax into a trivial insulator when freestanding.<sup>21</sup> Recently, the high-temperature phase,  $\beta$ -Bi<sub>4</sub>I<sub>4</sub>, has been confirmed by angle-resolved photoemission spectroscopy (ARPES)<sup>7</sup> to be a weak TI, whereas the low-temperature phase  $\alpha$ -Bi<sub>4</sub>I<sub>4</sub> has long been thought to be a trivial insulator, even using the state-of-the-art classification tools.<sup>3,22–24</sup> However, a more recent theoretical investigation predicts that  $\alpha$ -Bi<sub>4</sub>I<sub>4</sub> is a rare higher order TI<sup>6</sup> that hosts an insulating

Received: November 5, 2021

Revised: January 14, 2022

Published: January 25, 2022



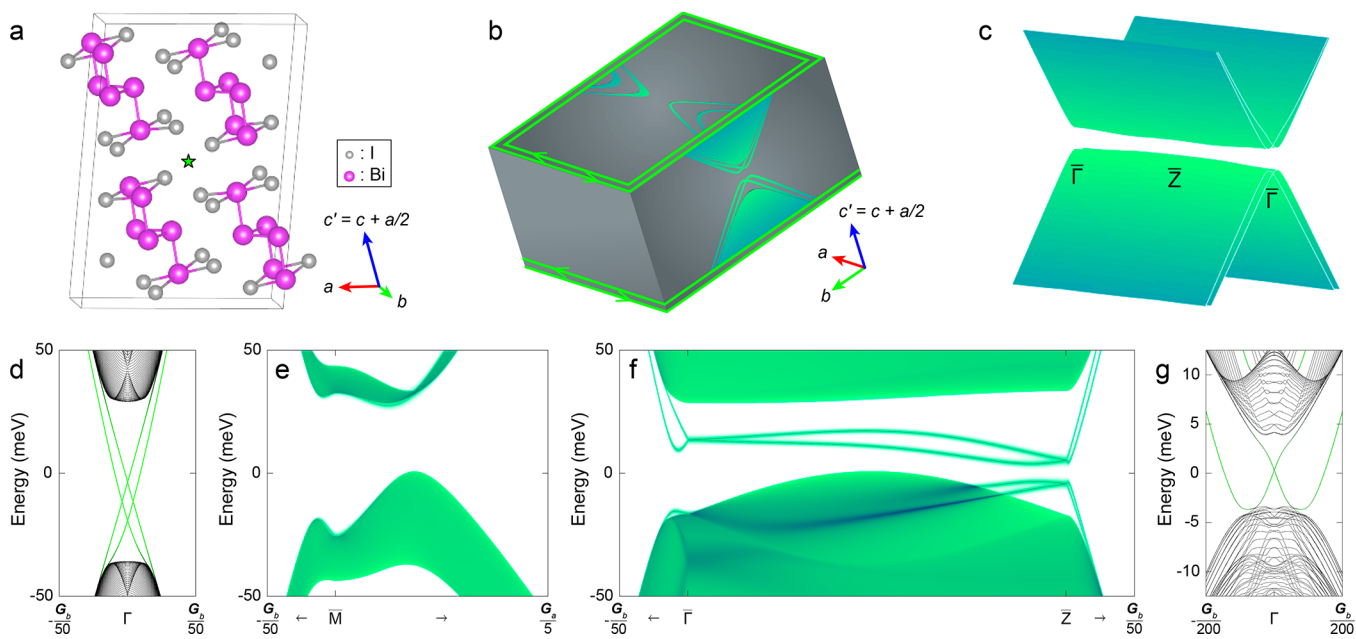


**Figure 1.** Band structure and characterization of bulk  $\text{Bi}_4\text{I}_4$  crystals. (a) Crystal structure of  $\alpha\text{-Bi}_4\text{I}_4$ . The gray box and green star are the conventional unit cell and inversion center, respectively. (b) Schematic of the higher order TI state of  $\alpha\text{-Bi}_4\text{I}_4$  with a particular surface termination. The bulk and surface bands are all gapped, and a helical hinge state around the top/bottom surface exists in the surface-state gap. (c) Zoom-in (100) side surface state in panel b featuring double Dirac cones with a small gap in the chain direction and a nearly vanishing dispersion in the stacking direction. (d) Edge-projected band structure of monolayer  $\alpha\text{-Bi}_4\text{I}_4$ . The green lines are the helical edge states at two parallel edges. (e) (001) surface-projected band structure of bulk  $\alpha\text{-Bi}_4\text{I}_4$ . No gapless surface states exist in the bulk gap. (f) (100) surface-projected band structure of bulk  $\alpha\text{-Bi}_4\text{I}_4$ . The green lines are the (100) side surface state in panel c. (g) Hinge-projected band structure of bulk  $\alpha\text{-Bi}_4\text{I}_4$ . The green lines are the hinge states along the chain direction in panel b, and the black lines are the (100) and  $(\bar{1}00)$  side surface states. Note that  $G_a$  and  $G_b$  are the reciprocal lattice vectors using the conventional unit cell notation and that the Miller indices are named using the  $a-b-c'$  notation. See the Supporting Information for computational details.

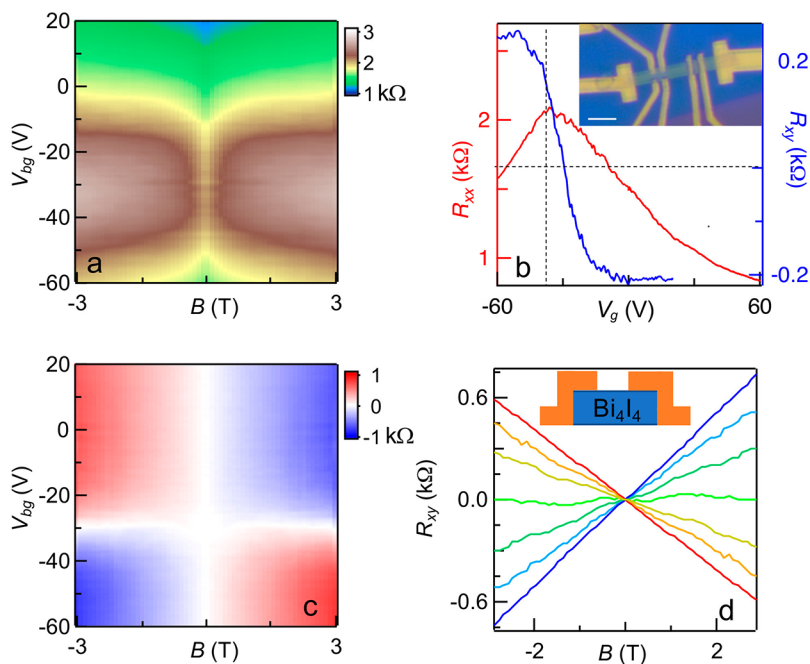


**Figure 2.** Magneto-transport data from device D1. (a)  $R_{xx}(V_g, B)$  at  $T = 1.8$  K. (b)  $R_{xx}(V_{bg})$  at  $B = 0$  and  $R_{xy}(V_{bg})$  at  $B = 1$  T. (Inset) Optical image of a device. Scale bar = 5  $\mu\text{m}$ . (c)  $R_{xy}(V_g, B)$  at  $T = 2$  K. (d)  $R_{xy}(B)$  at  $T = 1.7$  K for  $V_g = 20, -20, -25, -30, -35, -40$ , and  $-60$  V, respectively. (Inset) Schematic of the side view of device contacts (orange).

bulk state and gapped surface states (panels b, c, e, and f of Figure 1) yet gapless hinge states (panels b and g of Figure 1), which may be viewed as the time-reversal-invariant counterpart of the long-desired 3D quantum Hall effect<sup>25,26</sup> or the coupled-

edge-states counterpart of the celebrated Su–Schrieffer–Heeger model.<sup>6,27</sup>

Despite the rising interest in quasi-1D TIs in the community and the alluring prospects of  $\text{Bi}_4\text{I}_4$ , all experiments to date have

been performed on bulk materials.<sup>4,5,7,18,28–31</sup> However, to ultimately demonstrate the presence of non-trivial surface and hinge states and to leverage the room-temperature topological phase transition in  $\text{Bi}_4\text{I}_4$  as the topological switch between 2D surface and 1D hinge conductances, a demonstration of gate-tunable transport is of paramount importance. Here, we seek to explore the electronic properties of  $\text{Bi}_4\text{I}_4$  thin-film transistors. Bulk crystals are grown by the chemical vapor transport method. Although the  $\beta$  phase might be obtained at a low temperature via rapid quenching at high temperatures,<sup>5</sup> crystals that are cooled slowly from room temperature are observed to be in the  $\alpha$  phase.<sup>7</sup>

We fabricate thin-film  $\text{Bi}_4\text{I}_4$  field effect transistors, which are encapsulated by hexagonal BN (hBN) (see the *Supporting Information* for details of crystal growth and characterization, device fabrication, and computation techniques). An optical image of a  $\text{Bi}_4\text{I}_4$  device D1 is illustrated in the inset of Figure 2b, and the schematic of the device side view is shown in the inset of Figure 2d. The surface of the exfoliated sheet is the  $a-b$  plane, and the  $c$  axis is the out-of-plane direction. Panels a–c of Figure 2 display the longitudinal resistivity  $R_{xx}$  and Hall resistivity  $R_{xy}$  of device D1, which is  $\sim 25$  nm thick, as a function of the gate voltage  $V_g$  and magnetic field  $B$  at temperature  $T = 1.8$  K. The  $R_{xy}$  data are antisymmetrized with respect to  $B$  to remove artifacts induced by, e.g., slight misalignment between the Hall voltage probes. Transport is performed along the  $b$  axis, i.e., the atomic chain direction. Interestingly, both resistances are strongly gate-dependent. For instance, at  $B = 0$ , as the gate voltage increases from  $V_g = -60$  V,  $R_{xx}$  increases until it reaches a peak of  $\sim 2$  k $\Omega$  at  $V_{g,\text{max}} = -36.5$  V; for  $V_g > V_{g,\text{max}}$ ,  $R_{xx}$  continuously decreases and lowers to  $\sim 0.8$  k $\Omega$  at  $V_g = 60$  V (red curve and left axis of Figure 2b). This prominent  $R_{xx}$  peak in gate modulation is similar to those observed in Dirac materials, such as graphene,<sup>32</sup> 2D TIs, such as HgTe and InAs/GaSb quantum wells,<sup>33,34</sup> and the surface states of 3D TIs, such as  $\text{Bi}_2\text{Se}_3$ ,<sup>35,36</sup> and suggests the presence of a Dirac point or a very small band gap ( $k_{\text{B}}T \sim 0.15$  meV, where  $k_{\text{B}}$  is Boltzmann's constant); hence, we refer to the peak as "Dirac-like". Similarly,  $R_{xy}$  is strongly gate-tunable, becoming negative for  $V_g \gg V_{g,\text{max}}$  and positive for  $V_g \ll V_{g,\text{max}}$  indicating hole- and electron-dominated transport, respectively (blue curve and right axis of Figure 2b). For the entire range of gate voltage studied,  $R_{xy}$  is linear in  $B$ , as expected from the Drude model (Figure 2d). Thus, the strong gate dependence of  $R_{xx}$  and  $R_{xy}$ , together with the sign change in the latter, unambiguously establishes the presence of a gate-tunable channel in  $\alpha\text{-Bi}_4\text{I}_4$  transistors.

On the other hand, if the gate-tunable channel is the only conduction channel, we would expect that  $R_{xy}$  scales as  $1/(ne)$ , where  $n$  is the charge carrier density and  $e$  is the electron charge. Thus,  $R_{xy}$  should rapidly decrease once  $V_g$  is tuned past the Dirac-like peak in  $R_{xx}$ . However, in Figure 2b, for an extended range  $V_g > V_{g,\text{max}}$ ,  $R_{xy}$  remains almost constant, while  $R_{xx}$  steadily decreases; these behaviors are inconsistent with a single-carrier Drude model. To gain further insight into the transport properties of  $\text{Bi}_4\text{I}_4$ , we investigate the evolution of  $\rho_{xx}(V_g)$  at  $B = 0$  with the temperature for device D2, which is  $\sim 45$  nm thick (Figure 3a). Here, transport is performed along the  $a$  axis. Similar to device D1,  $R_{xx}$  is gate-tunable, with a resistivity peak at  $V_{g,\text{max}} \sim -48$  V. The collection of  $R_{xx}(V_g)$  curves taken at different temperatures, shown in the inset of Figure 3b, appears to cross at a single point,  $V_g = -6$  V and  $R_{xx} = 2$  k $\Omega$ ; for  $V_g < -6$  V ( $V_g > -6$  V),  $R$  decreases (increases)

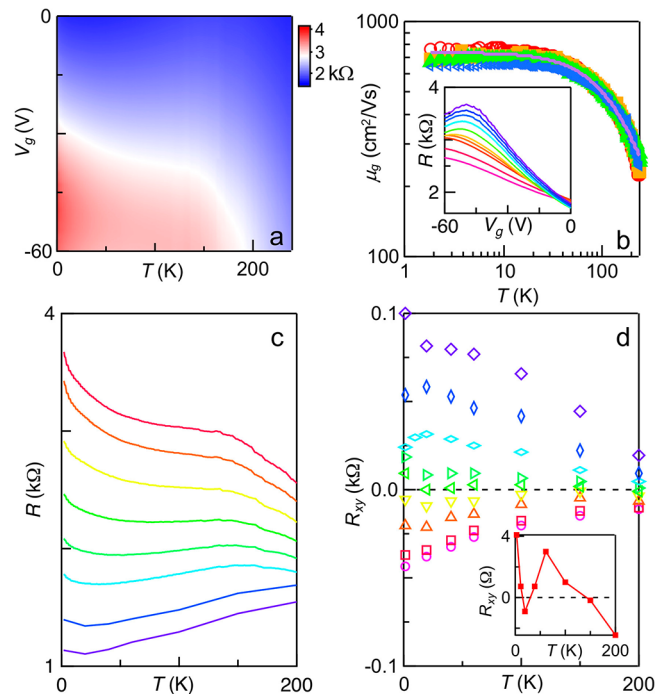


**Figure 3.** Temperature-dependent data from device D2. (a)  $R_{xx}(V_g, T)$  in k $\Omega$  taken at  $B = 0$ . (b) Mobility of the gate-tunable state, calculated using eq 1. The data sets are taken at  $(V_{g1}, V_{g2}) = (0, -5$  V),  $(-5, -10$  V),  $(-10, -15$  V), and  $(-15, -20$  V), respectively. The solid line is a fit to  $\mu_0/(1 + (T/A)^\alpha)$ , yielding  $\alpha = 1.5$  and  $\mu_0 \sim 730$   $\text{cm}^2 \text{V}^{-1} \text{s}^{-1}$ . (Inset)  $R_{xx}(V_g)$  at  $T = 2, 5, 10, 20, 40, 80, 120, 150, 180$ , and  $200$  K, respectively (from top to bottom). (c)  $R_{xx}(T)$  at  $V_g = -60, -40, -30, -20, -10, 0, 20$ , and  $40$  V, respectively (from top to bottom). (d)  $R_{xy}(T)$  at  $B = 1$  T and  $V_g = -60, -40, -30, -20, -15, -10, 0, 20$ , and  $40$  V (from top to bottom). (Inset)  $R_{xy}(T)$  at  $V_g = -14$  V, showing multiple sign changes as  $T$  decreases.  $R_{xx}$  and  $R_{xy}$  data are symmetrized and antisymmetrized with respect to  $B$ , respectively.

with increasing temperature, indicating insulating (metallic) transport. This metal–insulator transition-like behavior, driven by the gate voltage, is more clearly seen in Figure 3c, where  $R_{xx}(T)$  is plotted at different gate voltages. When the device is highly doped ( $V_g > 0$ ),  $dR_{xx}/dT > 0$  for most of the temperature range, except for a small resistivity uptick at  $T < 30$  K, suggesting a largely metallic regime. In contrast, when the device is close to the resistivity peak,  $dR_{xx}/dT < 0$  for the entire temperature range; the slope of the curve is steep near  $T \sim 200$  K, becoming almost flat between 135 and 75 K, and picks up again at low temperatures,  $T < 50$  K. Such variations in the slopes of the  $R_{xx}(T)$  curves suggest the presence of more than one transport mechanism. Another clue is given by the  $R_{xy}(T)$  curves at  $B = 1$  T for different gate voltages (Figure 3d), which are positive for  $V_g \sim V_{g,\text{max}}$  indicating hole-dominated transport, and negative for  $V_g \gg V_{g,\text{max}}$ . Taken together, we conclude that there are two competing transport mechanisms: an insulator-like bulk state that is hole-doped and an ambipolar metallic boundary state that can be tuned by  $V_g$ .

We note that the co-existence of bulk and boundary states can successfully account for the puzzlingly large variations in the temperature dependence of the resistance in bulk  $\text{Bi}_4\text{I}_4$  devices reported to date;<sup>5,29,30</sup> because the boundary state is sensitive to charge transfer, the variations in temperature dependence can be attributed to different doping levels of the boundary charges induced by, e.g., contaminants. Moreover, our data are also consistent with the observed multiple sign

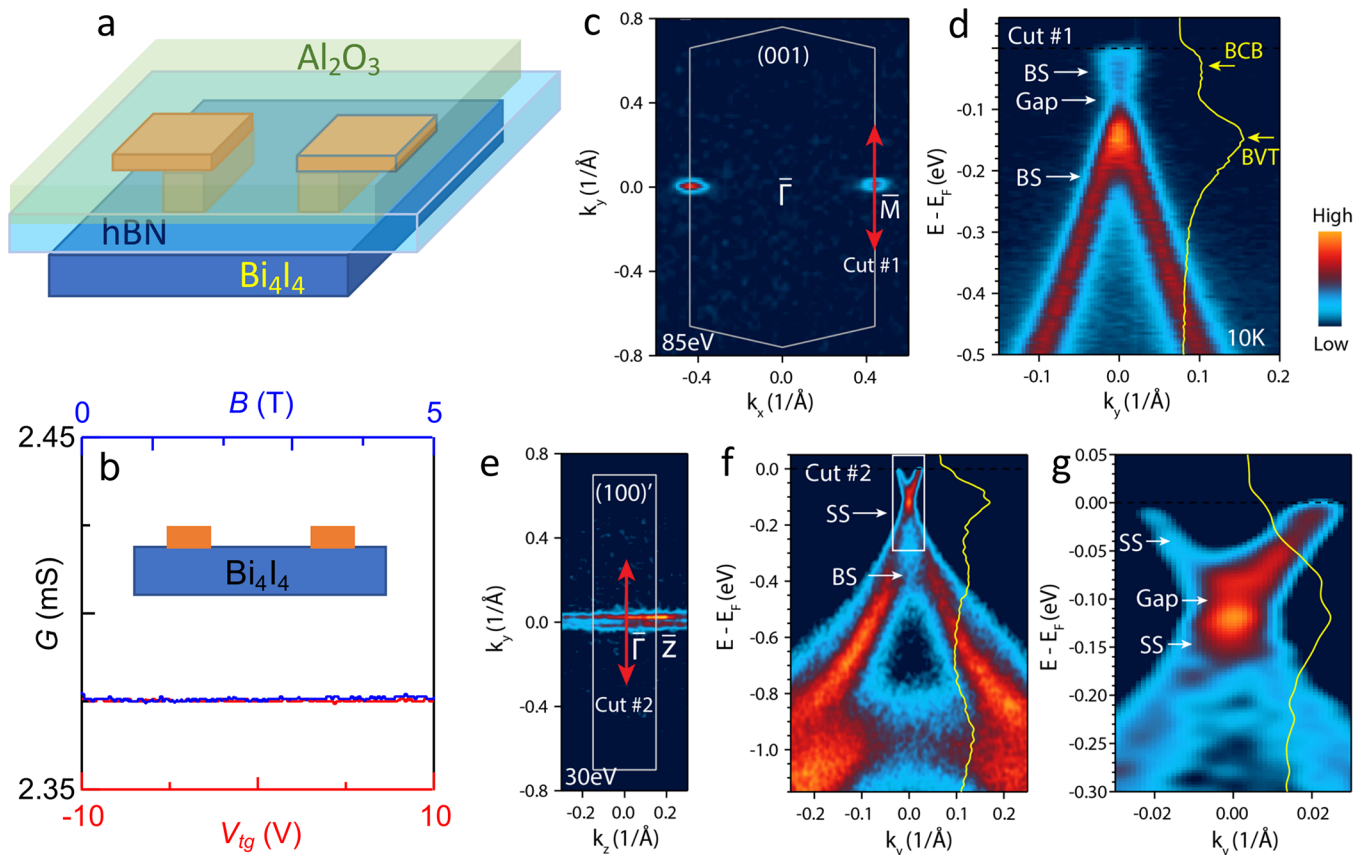


**Figure 4.** Transport and ARPES data excluding surface states on the  $a-b$  plane. (a) Schematic of a bulk-contacted device with top gate dielectric  $\text{Al}_2\text{O}_3$  and top gate (not shown). (b) Two-terminal conductance of a bulk-contacted device versus top gate voltage (bottom axis) and  $B$  (top axis). (Inset) Schematic of the side view of the device contacts. (c) Fermi surface mapping of  $\alpha\text{-Bi}_4\text{I}_4$  on the (001) top surface measured at 10 K with 85 eV photon energy. The gray frame represents the surface Brillouin zone. (d) Band image of cut 1 indicated in panel c. The white arrows mark the related bulk state (BS) and bulk band gap. The solid yellow line represents the energy distribution curve at  $k = 0$ . Related bulk valence band top (BVT) and bulk conduction band bottom (BCB) are marked by the yellow arrows. (e and f) Same as panels c and d but measured on the (100)' side surface. The photon energy was set to 30 eV to better resolve the surface states (SS). The arrows point to the BS and surface state (SS). (g) Zoom-in image of the boxed area in panel f. The arrows point to SS and a gap inside the SS.

changes in the  $R_{xy}(T)$  curve in one report,<sup>29</sup> if the device is nearly compensated, the competition between the hole-doped insulator-like bulk state and the electron-doped metallic boundary state results in sign changes as  $T$  is lowered. Indeed, this is observed in device D2 at  $V_g = -14$  V (inset of Figure 3d), where  $\rho_{xy}$  is negative at high and low temperatures yet positive at intermediate temperatures.

To delineate further bulk and boundary transport, we model the device conductivity by  $\sigma(V_g, T) = \sigma_g(V_g, T) + \sigma_b(T)$ , where  $\sigma_b$  and  $\sigma_g$  are conductivities of the bulk and gate-tunable channels, respectively. Because  $\sigma_b(T)$  is a constant at a given temperature, mobility of the gate-tunable channel can be extracted from the difference in total conductivity at different gate voltages

$$\mu_g(T) = \frac{\sigma(V_{g1}, T) - \sigma(V_{g2}, T)}{C_g(V_{g1} - V_{g2})} \quad (1)$$

where  $C_g$  is the capacitance between the gate and the boundary state. Using an estimated  $C_g \sim 11.8 \text{ nF/cm}^2$  for parallel plate capacitance between the flake and the Si back gate, we calculate  $\mu_g(T)$  from three different pairs of  $(V_{g1}, V_{g2})$  traces (Figure 3b). These curves collapse into a single trace, indicating that  $\mu_g$  is approximately independent of charge density. Because  $\mu_g$  has a power law scaling with the

temperature for phonon-dominated scattering at a high temperature and is nearly a constant for disorder-dominated scattering at a low temperature, we fit the curves to  $\mu_g = \mu_0 / (1 + (T/A)^\alpha)$ , where  $\mu_0$  and  $A$  are fitting parameters. With  $\alpha = 1.5$  and  $\mu_0 \sim 730 \text{ cm}^2 \text{ V}^{-1} \text{ s}^{-1}$ , the fits are in excellent agreement with data and consistent with phonon-dominated scattering for  $T > \sim 150$  K.

To summarize our observations thus far: (i) There is one or more gate-tunable transport channels in  $\alpha\text{-Bi}_4\text{I}_4$ . (ii) Transport through these channel(s) contribute to both longitudinal and Hall conductances. (iii) This channel is metallic and ambipolar, thus hosting either a Dirac point or a very small band gap. What is the origin of this gate-tunable state? A trivial mechanism is that it arises from a bulk band, which is lightly doped, so that charge density in the few bottommost layers is tuned by the back gate, while that deep in the bulk remains undisturbed as a result of screening. Alternatively, it originates from the top/bottom surface states on the  $a-b$  plane. To examine these possibilities, we note that these scenarios necessitate a top layer (or a few top layers) that conducts current uniformly. Thus, we fabricate a device with pre-patterned holes on the top hBN layer, so that contacts are only made to the interior (as opposed to the edge) of the top surface of a  $\text{Bi}_4\text{I}_4$  flake that is  $\sim 25$  nm in thickness. The device is completed by depositing  $\text{Al}_2\text{O}_3$  and a metal top gate. A

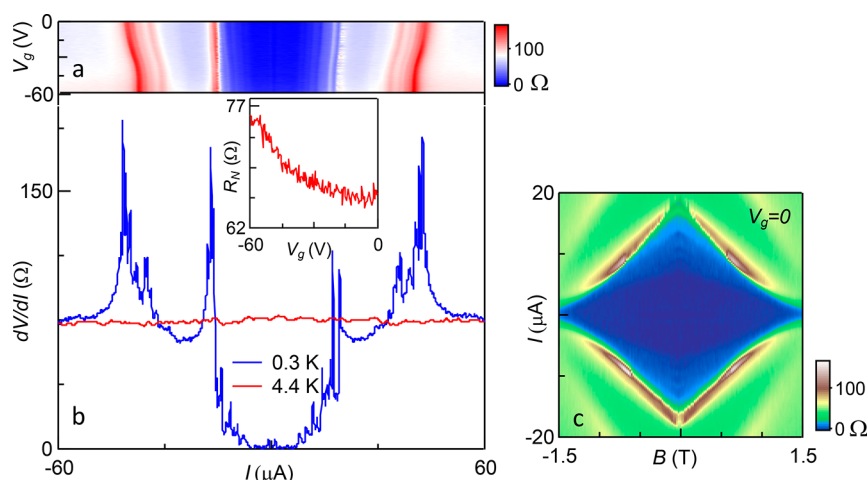


**Figure 5.** Supercurrent in a  $\text{Bi}_4\text{I}_4$  Josephson junction. (a) Differential resistance  $dV/dI$  in unit of  $\Omega$  versus bias current  $I$  and  $V_g$ . The dark blue region signifies the supercurrent. (b)  $dV/dI$  at  $V_g = 0$  and  $T = 0.3$  and  $4.4$  K, respectively. (Inset) Normal state resistance  $R_N(V_g)$ . (c)  $dV/dI$  in unit of  $\Omega$  versus  $I$  and  $B$  at  $V_g = 0$ , where  $B$  is perpendicular to the  $a-b$  plane.

schematic of this device is shown in Figure 4a. Resistance of such a device is  $\sim 2$   $\text{k}\Omega$ , indicating a conductive bulk and/or a conductive top surface. Here, the resistance is completely independent of the back gate voltage, top gate voltage, and magnetic field (Figure 4b), in sharp contrast to the data in Figures 2 and 3. This difference arises from regions at which the contacts are made: here, the contacts are made on the interior of the top surface (see the inset of Figure 4b), whereas contacts in the “standard” devices in Figures 2 and 3 cover both the interior and the edges (see the inset of Figure 2d). The gate independence of the interior-contacted device therefore excludes the bulk band and the top surface state as the origin of the gate-tunable channel; given the similarity of the top and bottom surface states, we also exclude the bottom surface state. The absence of surface states on the  $a-b$  plane is in fact consistent with first-principles calculations<sup>3</sup> (Figure 1e) and further verified by ARPES measurements on bulk crystals, as shown in panels c and d of Figure 4. There is no discernible surface state on the (001)  $a-b$  plane of  $\alpha\text{-Bi}_4\text{I}_4$ , where only a gapped bulk state is observed by ARPES at the surface Brillouin zone edge<sup>7</sup> (Figure 4c). Here, we can distinguish the (100) and (001) surfaces in the ARPES measurement by the distinct periodicity of the dispersions in momentum space, which is inversely proportional to the lattice constants  $a$  and  $c$  for the (001) and (100) surfaces, respectively.

Having eliminated the bulk band and the top/bottom surface states, we now discuss some non-trivial mechanisms for the gate-tunable transport in  $\alpha\text{-Bi}_4\text{I}_4$ . One such channel is the helical hinge states of  $\alpha\text{-Bi}_4\text{I}_4$  as a higher order TI<sup>3</sup> (panels b and g of Figure 1). A second possibility is the gapped surface states on the  $b-c'$  plane, i.e., on the sides of the device. The (100) surface state on the  $b-c'$  plane is seen in our calculated band structure<sup>3</sup> (panels b, c, and f of Figure 1) and in our ARPES data (panels e-g of Figure 4). Clearly, this (100) side surface state is a novel 2D electron system with a highly unusual structure;<sup>6,7</sup> while almost dispersionless in the  $c$  direction, it forms a massive Dirac band in the  $b$  direction. As a result of the large spin-orbit coupling and the local inversion symmetry breaking, the conduction and valence bands display quasi-1D Rashba-like spin splitting (Figure 1c). Both the side surface states and the helical hinge states can contribute to the longitudinal signal and be tunable by  $V_g$ ; however, they should

not contribute to the Hall resistance in our edge-contacted devices.

The gate tunable  $R_{xy}$  signals therefore suggest the presence of an additional channel. Here, we consider the last possibility, which is the 2D TI state that is expected to emerge in monolayer  $\text{Bi}_4\text{I}_4$ <sup>6</sup> (Figure 1d). On first glance, this possibility is rather surprising, because our devices are relatively thick. However, because the interlayer coupling in  $\text{Bi}_4\text{I}_4$  is extremely weak ( $\sim 10$  meV),<sup>6</sup> gate-induced charges accumulate primarily on the bottommost monolayer (or at most 2–3 layers as a result of screening), similar to that observed in gated bilayer  $\text{WSe}_2$  and  $\text{MoS}_2$ .<sup>37–40</sup> Albeit with a dissimilar dielectric environment and unrelaxed lattice constants compared to a freestanding monolayer,<sup>21</sup> this 2D TI state<sup>6</sup> hosts a gapped Dirac cone and, thus, contributes to both  $R_{xx}$  and  $R_{xy}$  signals.<sup>33,34</sup> The absence of conductance quantization is likely due to the presence of the conductive bulk or the surface/hinge states.

We therefore tentatively attribute the gate-tunable ambipolar channels to the bottommost 2D TI layer that is effectively decoupled from the upper layers, the gapped side surface states, and/or gapless hinge states around the upper layers. All of these channels are valuable platforms that afford rich physics, such as mediation of topological superconductivity. As a demonstration of this possibility, we couple a  $\text{Bi}_4\text{I}_4$  flake to  $\text{Ti}/\text{Nb}$  contacts that are separated by  $\sim 500$  nm. Figure 5a illustrates differential resistance  $dV/dI$  versus bias current  $I$  and  $V_g$ . Zero resistance states are observed; as  $I$  increases at  $0.3$  K, at least two pairs of sharp peaks are observed at  $\sim \pm 15$  and  $\sim \pm 40 \mu\text{A}$  (blue curve of Figure 5b), respectively, corresponding to the critical current  $I_c$  values of induced superconductivity with  $2\Delta_1 \sim 1.2$  meV and  $2\Delta_2 \sim 3$  meV, which are comparable to or less than the superconducting gap of Nb ( $2\Delta_{\text{bulk}} \sim 3$  meV). We note that these critical currents are considerably larger than those observed in graphene Josephson junctions with higher mobilities and similar device parameters.<sup>41–44</sup> Because  $I_c$  values are tunable by  $V_g$ , the supercurrent must be carried by the gate-tunable channels, consistent with our proposed mechanism. Moreover, the supercurrent is completely suppressed at  $4.4$  K (red curve of Figure 5b) or at a critical magnetic field of  $H_c \sim 2$  T perpendicular to the  $a-b$  plane (Figure 5c). We note that the Fraunhofer pattern is not

observed, because it is likely obscured by the supercurrent carried by the conductive bulk and possibly the side surface states. Additional experimental and theoretical investigation will be needed to fully elucidate the magnitude, nature, and mechanism of this exciting gate-tunable proximity-induced superconductivity.

In conclusion, we demonstrate gate-tunable transport in  $\alpha$ -Bi<sub>4</sub>I<sub>4</sub>, which is most consistent with the presence of gapped surface states on the  $b-c'$  plane, gapless edge states, and/or hinge states around the  $a-b$  plane. Emergence of the gate-tunable supercurrent mediated by these states provides a new avenue for creating and manipulating topological superconductivity and underscores the potential of quasi-1D TIs for realizing the promises of topological materials.

## ■ ASSOCIATED CONTENT

### SI Supporting Information

The Supporting Information is available free of charge at <https://pubs.acs.org/doi/10.1021/acs.nanolett.1c04264>.

Details of crystal synthesis, device fabrication, ARPES measurements, and computational methods ([PDF](#))

## ■ AUTHOR INFORMATION

### Corresponding Authors

Chun Ning Lau — Department of Physics, The Ohio State University, Columbus, Ohio 43210, United States;  
[ORCID.org/0000-0003-2159-6723](#); Email: [lau.232@osu.edu](mailto:lau.232@osu.edu)

Bing Lv — Department of Physics, The University of Texas at Dallas, Richardson, Texas 75080-3021, United States;  
[ORCID.org/0000-0002-9491-5177](#); Email: [blv@utdallas.edu](mailto:blv@utdallas.edu)

Fan Zhang — Department of Physics, The University of Texas at Dallas, Richardson, Texas 75080-3021, United States;  
[ORCID.org/0000-0003-4623-4200](#); Email: [zhang@utdallas.edu](mailto:zhang@utdallas.edu)

Ming Yi — Department of Physics and Astronomy, Rice University, Houston, Texas 77005, United States;  
Email: [mingyi@rice.edu](mailto:mingyi@rice.edu)

Robert J. Birgeneau — Department of Physics, University of California, Berkeley, Berkeley, California 94720, United States; Email: [robertjb@berkeley.edu](mailto:robertjb@berkeley.edu)

### Authors

Yulu Liu — Department of Physics, The Ohio State University, Columbus, Ohio 43210, United States

Ruoyu Chen — Department of Physics, The Ohio State University, Columbus, Ohio 43210, United States;  
[ORCID.org/0000-0002-4471-2574](#)

Zheneng Zhang — Department of Physics, The Ohio State University, Columbus, Ohio 43210, United States

Marc Bockrath — Department of Physics, The Ohio State University, Columbus, Ohio 43210, United States;  
[ORCID.org/0000-0002-7000-1442](#)

Yan-Feng Zhou — Department of Physics, The University of Texas at Dallas, Richardson, Texas 75080-3021, United States

Chiho Yoon — Department of Physics, The University of Texas at Dallas, Richardson, Texas 75080-3021, United States;  
Department of Physics and Astronomy, Seoul National University, Seoul 08826, Korea

Sheng Li — Department of Physics, The University of Texas at Dallas, Richardson, Texas 75080-3021, United States

Xiaoyuan Liu — Department of Physics, The University of Texas at Dallas, Richardson, Texas 75080-3021, United States

Nikhil Dhale — Department of Physics, The University of Texas at Dallas, Richardson, Texas 75080-3021, United States

Kenji Watanabe — Research Center for Functional Materials, National Institute for Materials Science, Tsukuba 305-0044, Japan; [ORCID.org/0000-0003-3701-8119](#)

Takashi Taniguchi — International Center for Materials Nanoarchitectonics, National Institute for Materials Science, Tsukuba 305-0044, Japan; [ORCID.org/0000-0002-1467-3105](#)

Jianwei Huang — Department of Physics and Astronomy, Rice University, Houston, Texas 77005, United States

Ji Seop Oh — Department of Physics, University of California, Berkeley, Berkeley, California 94720, United States

Complete contact information is available at:  
<https://pubs.acs.org/10.1021/acs.nanolett.1c04264>

### Notes

The authors declare no competing financial interest.

## ■ ACKNOWLEDGMENTS

This work is mainly supported by the National Science Foundation (NSF) through the DMREF program. The work at The Ohio State University (OSU) is supported by NSF under Grant DMR-1922076. The work at The University of Texas at Dallas (UTD) is supported by NSF under Grants DMR-1921581 and DMR-1945351 and the Army Research Office (ARO) under Grant W911NF-18-1-0416. The work at Rice is supported by NSF under Grant DMR-1921847. The work at the University of California, Berkeley (UCB) is supported by NSF Grant 1921798. Device fabrication is performed in the NanoSystems Laboratory (NSL) cleanroom, which is supported by the Center for Emergent Materials (CEM), a NSF Materials Research Science and Engineering Center (MRSEC) (2011876). Sheng Li, Xiaoyuan Liu, Nikhil Dhale, and Bing Lv also acknowledge the support by the Air Force Office of Scientific Research (AFOSR) under Grant FA9550-19-1-0037. Jianwei Huang and Ming Yi also acknowledge the support of the Robert A. Welch Foundation Grant No. C-2024, and the Gordon and Betty Moore Foundation's EPiQS Initiative through grant no. GBMF9470. Kenji Watanabe and Takashi Taniguchi acknowledge support from the Elemental Strategy Initiative conducted by the Ministry of Education, Culture, Sports, Science and Technology (MEXT), Japan, Grant JPMXP0112101001, Japan Society for the Promotion of Science (JSPS) Grants-in-Aid for Scientific Research (KAKENHI) Grant JP20H00354, and the Core Research for Evolutional Science and Technology (CREST) (JPMJCR15F3), Japan Science and Technology Agency (JST). Yan-Feng Zhou, Chiho Yoon, and Fan Zhang acknowledge the Texas Advanced Computing Center (TACC) for providing resources that have contributed to the research results reported in this work.

## ■ REFERENCES

- (1) Qi, X.-L.; Zhang, S.-C. Topological insulators and superconductors. *Rev. Mod. Phys.* **2011**, *83*, 1057.

(2) Hasan, M. Z.; Kane, C. L. Colloquium: Topological insulators. *Rev. Mod. Phys.* **2010**, *82*, 3045.

(3) Liu, C.-C.; Zhou, J.-J.; Yao, Y.; Zhang, F. Weak Topological Insulators and Composite Weyl Semimetals:  $\beta$ -Bi<sub>4</sub>X<sub>4</sub> (X = Br, I). *Phys. Rev. Lett.* **2016**, *116*, 066801.

(4) Autès, G.; Isaeva, A.; Moreschini, L.; Johannsen, J. C.; Pisoni, A.; Mori, R.; Zhang, W.; Filatova, T. G.; Kuznetsov, A. N.; Forró, L.; Van den Broek, W.; Kim, Y.; Kim, K. S.; Lanzara, A.; Denlinger, J. D.; Rotenberg, E.; Bostwick, A.; Grioni, M.; Yazev, O. V. A novel quasi-one-dimensional topological insulator in bismuth iodide  $\beta$ -Bi<sub>4</sub>I<sub>4</sub>. *Nat. Mater.* **2016**, *15*, 154.

(5) Noguchi, R.; Takahashi, T.; Kuroda, K.; Ochi, M.; Shirasawa, T.; Sakano, M.; Bareille, C.; Nakayama, M.; Watson, M. D.; Yaji, K.; Harasawa, A.; Iwasawa, H.; Dudin, P.; Kim, T. K.; Hoesch, M.; Kandyba, V.; Giampietri, A.; Barinov, A.; Shin, S.; Arita, R.; Sasagawa, T.; Kondo, T. A weak topological insulator state in quasi-one-dimensional bismuth iodide. *Nature* **2019**, *566*, 518.

(6) Yoon, C.; Liu, C.-C.; Min, H.; Zhang, F. Quasi-One-Dimensional Higher-Order Topological Insulators. *arXiv.org, e-Print Arch., Condens. Matter* **2020**, arXiv:2005.14710.

(7) Huang, J.; Li, S.; Yoon, C.; Oh, J. S.; Wu, H.; Liu, X.; Dhale, N.; Zhou, Y.-F.; Guo, Y.; Zhang, Y.; Hashimoto, M.; Lu, D.; Denlinger, J.; Wang, X.; Lau, C. N.; Birgeneau, R. J.; Zhang, F.; Lv, B.; Yi, M. Room-Temperature Topological Phase Transition in Quasi-One-Dimensional Material Bi<sub>4</sub>I<sub>4</sub>. *Phys. Rev. X* **2021**, *11*, 031042.

(8) Noguchi, R.; Kobayashi, M.; Jiang, Z.; Kuroda, K.; Takahashi, T.; Xu, Z.; Lee, D.; Hirayama, M.; Ochi, M.; Shirasawa, T.; Zhang, P.; Lin, C.; Bareille, C.; Sakuragi, S.; Tanaka, H.; Kunisada, S.; Kurokawa, K.; Yaji, K.; Harasawa, A.; Kandyba, V.; Giampietri, A.; Barinov, A.; Kim, T. K.; Cacho, C.; Hashimoto, M.; Lu, D.; Shin, S.; Arita, R.; Lai, K.; Sasagawa, T.; Kondo, T. Evidence for a higher-order topological insulator in a three-dimensional material built from van der Waals stacking of bismuth-halide chains. *Nat. Mater.* **2021**, *20*, 473.

(9) Ando, Y. Topological Insulator Materials. *J. Phys. Soc. Jpn.* **2013**, *82*, 102001.

(10) Bansil, A.; Lin, H.; Das, T. Colloquium: Topological band theory. *Rev. Mod. Phys.* **2016**, *88*, 021004.

(11) Hasan, M. Z.; Xu, S.-Y.; Bian, G. Topological insulators, topological superconductors and Weyl fermion semimetals: Discoveries, perspectives and outlooks. *Phys. Scr.* **2015**, *2015*, 014001.

(12) Hsieh, D.; Qian, D.; Wray, L.; Xia, Y.; Hor, Y. S.; Cava, R. J.; Hasan, M. Z. A topological Dirac insulator in a quantum spin Hall phase. *Nature* **2008**, *452*, 970.

(13) Teo, J. C. Y.; Kane, C. L. Topological defects and gapless modes in insulators and superconductors. *Phys. Rev. B* **2010**, *82*, 115120.

(14) Zhang, H.; Liu, C.-X.; Qi, X.-L.; Dai, X.; Fang, Z.; Zhang, S.-C. Topological insulators in Bi<sub>2</sub>Se<sub>3</sub>, Bi<sub>2</sub>Te<sub>3</sub> and Sb<sub>2</sub>Te<sub>3</sub> with a single Dirac cone on the surface. *Nat. Phys.* **2009**, *5*, 438.

(15) Xia, Y.; Qian, D.; Hsieh, D.; Wray, L.; Pal, A.; Lin, H.; Bansil, A.; Grauer, D.; Hor, Y. S.; Cava, R. J.; Hasan, M. Z. Observation of a large-gap topological-insulator class with a single Dirac cone on the surface. *Nat. Phys.* **2009**, *5*, 398.

(16) Chen, Y. L.; Analytis, J. G.; Chu, J.-H.; Liu, Z. K.; Mo, S.-K.; Qi, X. L.; Zhang, H. J.; Lu, D. H.; Dai, X.; Fang, Z.; Zhang, S. C.; Fisher, I. R.; Hussain, Z.; Shen, Z.-X. Experimental Realization of a Three-Dimensional Topological Insulator, Bi<sub>2</sub>Te<sub>3</sub>. *Science* **2009**, *325*, 178.

(17) Dikarev, E. V.; Popovkin, B. A.; Shevelkov, A. V. New polymolecular bismuth monohalides. Synthesis and crystal structures of Bi<sub>4</sub>Br<sub>x</sub>I<sub>4-x</sub> (x = 1, 2, or 3). *Russian Chemical Bulletin* **2001**, *50*, 2304.

(18) Filatova, T. G.; Gurin, P. V.; Kloo, L.; Kulbachinskii, V. A.; Kuznetsov, A. N.; Kytin, V. G.; Lindsjo, M.; Popovkin, B. A. Electronic structure, galvanomagnetic and magnetic properties of the bismuth subhalides Bi<sub>4</sub>I<sub>4</sub> and Bi<sub>4</sub>Br<sub>4</sub>. *J. Solid State Chem.* **2007**, *180*, 1103.

(19) von Schnering, H. G.; von Benda, H.; Kalveram, C. Wismutmonoiodid BiI<sub>3</sub>, eine Verbindung mit Bi(O) und Bi(II). *Z. Anorg. Allg. Chem.* **1978**, *438*, 37.

(20) Weiz, A.; Anh, M. L.; Kaiser, M.; Rasche, B.; Herrmannsdörfer, T.; Doert, T.; Ruck, M. Optimized Synthesis of the Bismuth Subiodides Bi<sub>m</sub>I<sub>4</sub> (m = 4, 14, 16, 18) and the Electronic Properties of Bi<sub>14</sub>I<sub>4</sub> and Bi<sub>18</sub>I<sub>4</sub>. *Eur. J. Inorg. Chem.* **2017**, *2017*, 5609.

(21) Zhou, J.-J.; Feng, W.; Liu, C.-C.; Guan, S.; Yao, Y. Large-Gap Quantum Spin Hall Insulator in Single Layer Bismuth Monobromide Bi<sub>4</sub>Br<sub>4</sub>. *Nano Lett.* **2014**, *14*, 4767.

(22) Zhang, T.; Jiang, Y.; Song, Z.; Huang, H.; He, Y.; Fang, Z.; Weng, H.; Fang, C. Catalogue of topological electronic materials. *Nature* **2019**, *566*, 475.

(23) Vergniory, M. G.; Elcoro, L.; Felser, C.; Regnault, N.; Bernevig, B. A.; Wang, Z. A complete catalogue of high-quality topological materials. *Nature* **2019**, *566*, 480.

(24) Tang, F.; Po, H. C.; Vishwanath, A.; Wan, X. Comprehensive search for topological materials using symmetry indicators. *Nature* **2019**, *566*, 486.

(25) Halperin, B. I. Possible States for a Three-Dimensional Electron Gas in a Strong Magnetic Field. *Jpn. J. Appl. Phys.* **1987**, *26*, 1913.

(26) Tang, F.; Ren, Y.; Wang, P.; Zhong, R.; Schneloch, J.; Yang, S. A.; Yang, K.; Lee, P. A.; Gu, G.; Qiao, Z.; Zhang, L. Three-dimensional quantum Hall effect and metal–insulator transition in ZrTe<sub>5</sub>. *Nature* **2019**, *569*, 537.

(27) Su, W. P.; Schrieffer, J. R.; Heeger, A. J. Solitons in Polyacetylene. *Phys. Rev. Lett.* **1979**, *42*, 1698.

(28) Qi, Y.; Shi, W.; Werner, P.; Naumov, P. G.; Schnelle, W.; Wang, L.; Rana, K. G.; Parkin, S.; Medvedev, S. A.; Yan, B.; Felser, C. Pressure-induced superconductivity and topological quantum phase transitions in a quasi-one-dimensional topological insulator: Bi<sub>4</sub>I<sub>4</sub>. *npj Quantum Mater.* **2018**, *3*, 4.

(29) Pisoni, A.; Gaál, R.; Zeugner, A.; Falkowski, V.; Isaeva, A.; Huppertz, H.; Autès, G.; Yazev, O. V.; Forró, L. Pressure effect and superconductivity in the  $\beta$ -Bi<sub>4</sub>I<sub>4</sub> topological insulator. *Phys. Rev. B* **2017**, *95*, 235149.

(30) Chen, D.-Y.; Ma, D.-S.; Li, Y.; Du, Z. Z.; Xiong, X.; He, Y.; Duan, J.; Han, J.; Chen, D.; Xiao, W.; Yao, Y. Quantum transport properties in single crystals of  $\alpha$ -Bi<sub>4</sub>I<sub>4</sub>. *Phys. Rev. Mater.* **2018**, *2*, 114408.

(31) Li, X.; Chen, D.; Jin, M.; Ma, D.; Ge, Y.; Sun, J.; Guo, W.; Sun, H.; Han, J.; Xiao, W.; Duan, J.; Wang, Q.; Liu, C.-C.; Zou, R.; Cheng, J.; Jin, C.; Zhou, J.; Goodenough, J. B.; Zhu, J.; Yao, Y. Pressure-induced phase transitions and superconductivity in a quasi-1-dimensional topological crystalline insulator  $\alpha$ -Bi<sub>4</sub>Br<sub>4</sub>. *Proc. Nat. Acad. Sci.* **2019**, *116*, 17696.

(32) Novoselov, K. S.; Geim, A. K.; Morozov, S. V.; Jiang, D.; Zhang, Y.; Dubonos, S. V.; Grigorieva, I. V.; Firsov, A. A. Electric field effect in atomically thin carbon films. *Science* **2004**, *306*, 666.

(33) Brüne, C.; Roth, A.; Buhmann, H.; Hankiewicz, E. M.; Molenkamp, L. W.; Maciejko, J.; Qi, X.-L.; Zhang, S.-C. Spin polarization of the quantum spin Hall edge states. *Nat. Phys.* **2012**, *8*, 485.

(34) Knez, I.; Du, R.-R.; Sullivan, G. Evidence for Helical Edge Modes in Inverted InAs/GaSb Quantum Wells. *Phys. Rev. Lett.* **2011**, *107*, 136603.

(35) Checkelsky, J. G.; Hor, Y. S.; Cava, R. J.; Ong, N. P. Bulk Band Gap and Surface State Conduction Observed in Voltage-Tuned Crystals of the Topological Insulator Bi<sub>2</sub>Se<sub>3</sub>. *Phys. Rev. Lett.* **2011**, *106*, 196801.

(36) Kim, D.; Cho, S.; Butch, N. P.; Syers, P.; Kirshenbaum, K.; Adam, S.; Paglione, J.; Fuhrer, M. S. Surface conduction of topological Dirac electrons in bulk insulating Bi<sub>2</sub>Se<sub>3</sub>. *Nat. Phys.* **2012**, *8*, 459.

(37) Fallahazad, B.; Movva, H. C. P.; Kim, K.; Larentis, S.; Taniguchi, T.; Watanabe, K.; Banerjee, S. K.; Tutuc, E. Shubnikov–de Haas Oscillations of High-Mobility Holes in Monolayer and Bilayer WSe<sub>2</sub>: Landau Level Degeneracy, Effective Mass, and Negative Compressibility. *Phys. Rev. Lett.* **2016**, *116*, 086601.

(38) Movva, H. C. P.; Fallahazad, B.; Kim, K.; Larentis, S.; Taniguchi, T.; Watanabe, K.; Banerjee, S. K.; Tutuc, E. Density-Dependent Quantum Hall States and Zeeman Splitting in Monolayer and Bilayer MoS<sub>2</sub>. *Phys. Rev. Lett.* **2017**, *118*, 247701.

(39) Lin, J.; Han, T.; Piot, B. A.; Wu, Z.; Xu, S.; Long, G.; An, L.; Cheung, P.; Zheng, P.-P.; Plochocka, P.; Dai, X.; Maude, D. K.; Zhang, F.; Wang, N. Determining Interaction Enhanced Valley Susceptibility in Spin-Valley-Locked MoS<sub>2</sub>. *Nano Lett.* **2019**, *19*, 1736.

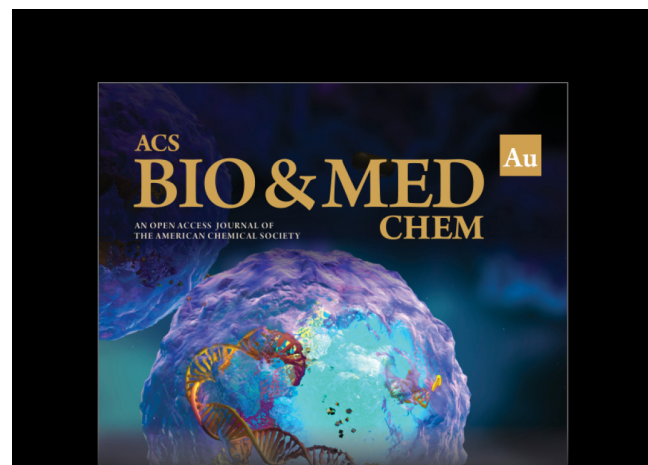
(40) Pisoni, R.; Davatz, T.; Watanabe, K.; Taniguchi, T.; Ihn, T.; Ensslin, K. Absence of Interlayer Tunnel Coupling of K-Valley Electrons in Bilayer MoS<sub>2</sub>. *Phys. Rev. Lett.* **2019**, *123*, 117702.

(41) Amet, F.; Ke, C. T.; Borzenets, I. V.; Wang, J.; Watanabe, K.; Taniguchi, T.; Deacon, R. S.; Yamamoto, M.; Bomze, Y.; Tarucha, S.; Finkelstein, G. Supercurrent in the quantum Hall regime. *Science* **2016**, *352*, 966.

(42) Calado, V. E.; Goswami, S.; Nanda, G.; Diez, M.; Akhmerov, A. R.; Watanabe, K.; Taniguchi, T.; Klapwijk, T. M.; Vandersypen, L. M. K. Ballistic Josephson junctions in edge-contacted graphene. *Nat. Nanotechnol.* **2015**, *10*, 761.

(43) Du, X.; Skachko, I.; Andrei, E. Y. Josephson current and multiple Andreev reflections in graphene SNS junctions. *Phys. Rev. B* **2008**, *77*, 184507.

(44) Ben Shalom, M.; Zhu, M. J.; Fal'ko, V. I.; Mishchenko, A.; Kretinin, A. V.; Novoselov, K. S.; Woods, C. R.; Watanabe, K.; Taniguchi, T.; Geim, A. K.; Prance, J. R. Quantum oscillations of the critical current and high-field superconducting proximity in ballistic graphene. *Nat. Phys.* **2016**, *12*, 318.



Editor-in-Chief: **Prof. Shelley D. Minteer**, University of Utah, USA



Deputy Editor  
**Prof. Squire J. Booker**  
Pennsylvania State University, USA

**Open for Submissions** 

pubs.acs.org/biomedchemau  ACS Publications  
Most Trusted. Most Cited. Most Read.